International Forum on Aeroelasticity and Structural Dynamics
IFASD 2024
17-21 June 2024, The Hague, The Netherlands

EXPLORING THE EFFECT OF DIFFERENT SHOCK IMPINGEMENT ANGLES ON AEROELASTIC RESPONSE FOR A THIN PANEL

Luisa Piccolo Serafim[1] **and Earl Dowell**[1]

[1]Duke University
Durham, North Carolina USA
luisa.piccolo.serafim@duke.edu

Keywords: Fluid-Structural Interaction (FSI), shock impingement, Limit Cycle Oscillation (LCO), Aeroelasticity

Abstract: In this study, a novel dynamically linearized Euler time-domain approach is used to compute the generalized aerodynamic force from a CFD simulation. The aerodynamic forcing term is implemented in a theoretical/computational nonlinear aeroelastic model to assess the dynamic response of a flexible clamped-clamped panel considering the pressure profile due to different shock wedge angles. One benefit of this approach is the possibility to perform the same analysis to solve the Navier-Stokes Equation via RANS simulation and consider the viscous boundary layer effect for near transonic regimes. Different shock wedge configurations will be explored in this study in the CFD/ROM simulation and the aeroelastic solution using an inviscid solver. These results will also be compared with the same structural configuration considering a modified Piston Theory model, exploring the limitations and opportunities of this simpler and faster solution.

NOMENCLATURE

a, b, h	panel length, width, and thickness, respectively
$Q_{m,k}$	generalized aerodynamic force
$q_m, \dot{q}_m$	generalized coordinates for displacement and velocity, respectively
w	physical panel deformation
$\hat{w}$	physical dynamic panel deformation around the mean deformation ($\bar{w}(t)$)
M_∞	Mach number
p_∞	free stream static pressure
U_∞	free stream velocity
ρ_∞	free stream density
λ^*	nondimensional dynamic pressure ($\lambda^* = \rho U_\infty^2 a^3/D$)
x, y and z	spatial coordinates
t	time
ψ_m	structural modes
χ	(small) amplitude for panel deformation
f, ω	frequency in Hz and rad/s, respectively
k	reduced frequency ($k = \omega a/U_\infty$)

1 INTRODUCTION

Shock-Wave/Boundary-Layer Interactions (SWBLI) in supersonic and hypersonic flows is a topic that is usually explored experimentally or computationally using CFD when it comes to aeroelastic instabilities [1–3]. The importance of this topic is understanding the physical aspects of the phenomenon and what it means for the structural integrity of the aircraft during flight. Brouwer et al. and Spottswood et al. developed and presented a detailed benchmark for a supersonic wind tunnel measurement, for configurations with and without shock impingement, [1, 4–6]. Different shock wedge angles allowed the visualization of attached and bubble separation during the elastic deformation of the thin clamped-clamped panel, besides proving a thorough benchmark for aeroelasticians to perform numerical simulations, [7, 8]. The clamped-free configuration is also explored by aeroelastic experimentalists in different Mach numbers by Curral et al. and Vasconcelos et al., [9, 10].

The analytical (and/or numerical) implementation of nonlinear aerodynamic behavior into the aeroelastic solution has always been a challenge in the field of fluid-structure interactions mainly because of the time scale difference between the fluid and structural solver. Configurations with shock impingement case and/or viscous boundary layer presents a more challenging scenario where the expected simplified assumptions, i.e. isentropic inviscid flows, can no longer be applied. For an elastic plate, the traditional aerodynamic method in a supersonic aeroelastic analysis is the Linear Piston Theory (LPT), which is known to be a good approximation for $M_\infty \approx 2.0$ and above. However, the LPT is limited in terms of the Mach number considered in the analysis, the neglect of the 3D effect in the unsteady flow behavior, and the assumption of uniform flow over the panel surface. In other words, using this linear and local LPT model does not include the nonlinearity of more complex flows, such as configurations with shock impingement or near-transonic regimes.

An extended (or improved) version of the Piston Theory (Enriched Piston Theory) was developed by Brouwer and McNamara [11] and has already been shown to model the local pressure obtained by experimental results [12]. The Enriched Piston Theory is based on CFD steady-state training data, such as RANS, to account for the flow nonlinearities. By doing so, it provides the aeroelastic response faster than the direct implementation of the two-way coupled fluid-structural model. Using CFD time marching FSI simulations, Boyer et al. and Visbal et al. explored the modeling of inviscid and viscous implementations on a pinned-pinned square plate, [13–15]. They discussed the implications of solving a two- or three-dimensional shock impingement problem, as well as the effects of different pressure ratios before and after the shock impingement on the aeroelastic solution. Laguarda et al. [16] also explored FSI with a flexible panel including an oblique shock and the turbulent boundary layer effect using a loosely coupled implementation. Johnson et al. [17] go one step further implementing wall-modeled large eddy simulation (WMLES) to assess the effect of fluctuation pressure on the aeroelastic solution using a one-way coupled method with an analytical structural model. The dominant parameters in the solution are characterized and the authors identify the sensibility of the aeroelastic model to the LES-rich flow information. Although the latter is still limited by the time scale required to run an LES solution, the advantage of this method is the simpler implementation of the coupling step between fluid and structure.

The advantage of solving FSI problems using a combination of numerical and analytical methods is the possibility of exploring different configurations and their sensibility to different parameters at a faster pace than when using a numerical solver only. For similar reasons, the development of Reduced Order Model (ROM) methods combining these two approaches in the

aeroelastic context has been an important goal in the field. Among the many ROM options available in the literature, including the Enriched Piston theory previously mentioned, the Indicial Response offers a good performance in capturing some aerodynamic nonlinearities to be included in the modeling process, both for simple and complex geometries [18]. The present authors made use of the Dynamic Linearized Time-domain Approach (DLTA) [19] to assess different shock configurations on an elastic panel and compare the solution performance using a modified version of Piston Theory. This new approach is based on the Indicial Theory, where the unsteady flow is modeled with a linear behavior (due to a small perturbation to the system) about a nonlinear steady state of the flow. Once this "linear" information is obtained from a numerical solution, i.e. CFD model, the generalized aerodynamic force in the aeroelastic solution is reconstructed inside the aeroelastic solver, as a function of the Mach number, the structural boundary conditions, and the mean aerodynamic conditions [20].

The goal of this study is to explore the capabilities of this method when solving a problem with shock impingement acting on the flexible panel. One can argue that, for systems with shock impingement, viscosity can play an important role in the dynamic of the panel, and the authors agree with this statement. Still, in the present paper, the numerical solver is chosen to be inviscid (Euler) to facilitate the interpretation of the results as a function of the shock impingement only, and the cases selected were based on previous experimental configurations where Shock-Wave/Boundary-Layer Interactions (SWBL) results were not found [1]. Another goal of this study is to explore the contribution of the steady forcing term due to a static pressure differential on the panel dynamic response.

2 THEORETICAL MODEL

2.1 Structural Model

The structural model in this study was based on the nonlinear von Karman plate equations, presented in detail in [21, 22]. The boundary conditions of the elastic plate in this study assume all four edges of the panel to be fully clamped, enforcing no in-plane displacement on the structure at the plate boundary. The mode shapes assumed in the study are presented in Eq. 1. Note that in Eqs. 2 and 3, the first root is zero, so $m = 2$ is the first mode shape of the clamped beam. For the y-direction, the shape function was shifted half the width of the panel, in order to have the central line the x-axis, [23]

$$\begin{aligned}
\psi_m &= \cos\left[\gamma_{1_m}\left(\frac{x}{a}-\frac{1}{2}\right)\right] + \frac{\sin\left(\gamma_{1_m}/2\right)}{\sinh\left(\gamma_{1_m}/2\right)}\cosh\left[\gamma_{1_m}\left(\frac{x}{a}-\frac{1}{2}\right)\right], \quad m = 2,4,6,\ldots \\
\psi_m &= \sin\left[\gamma_{2_m}\left(\frac{x}{a}-\frac{1}{2}\right)\right] - \frac{\sin\left(\gamma_{2_m}/2\right)}{\sinh\left(\gamma_{2_m}/2\right)}\sinh\left[\gamma_{2_m}\left(\frac{x}{a}-\frac{1}{2}\right)\right], \quad m = 3,5,7,\ldots
\end{aligned} \tag{1}$$

where γ_{1_m} is the $m/2$-th root of

$$\tan\left(\frac{\gamma_{1_m}}{2}\right) + \tanh\left(\frac{\gamma_{1_m}}{2}\right) = 0, \tag{2}$$

and γ_{2_m} is the $(m-1)/2$-th root of

$$\tan\left(\frac{\gamma_{2_m}}{2}\right) - \tanh\left(\frac{\gamma_{2_m}}{2}\right) = 0. \tag{3}$$

2.2 Dynamically Linearized Domain Approach (DLTA)

The Dynamically Linearized Time-domain Approach [19] is based on the assumption that, given a small magnitude of a known structural displacement experienced by the elastic panel, one can model the generalized aerodynamic force by the linear expression presented in Eq. 4:

$$Q_{m,k}(t) = q_m(t)A_{m,k} + \dot{q}_m(t)B_{m,k} + \int_0^t q_m(\tau)E_{m,k}(t-\tau)d\tau \tag{4}$$

The $A_{m,k}$, $B_{m,k}$, and $E_{m,k}(t)$ matrices are determined for a given set of aerodynamic parameters, e.g. Mach number, etc. Also, Eq. 4 is valid for small panel deformations compared to the panel chord, which is true for the clamped-clamped configuration. Because of structural nonlinearities, the panel deformation is restricted to be in the order of its thickness before any structural failure. The same may not be true for a clamped-free configuration, however. The deformation expected for this second case is on the order of the panel length for the aeroelastic instability, which may lead to nonlinear aerodynamic behavior, even with a uniform freestream.

For each m structural mode required, a CFD solution is run using a known enforced motion to the structure with a small amplitude deformation (χ) to obtain an unsteady distribution, represented in Eq. 5 as $\Delta p_m(x, y, t)$.

$$Q_{m,k}\left(t\right) = \iint \frac{\left(p_m\left(x,y,t\right) - p_\infty\right)}{\rho_\infty U_\infty^2}\psi_k\left(x,y\right)\mathrm{d}y\mathrm{d}x = \iint \frac{\Delta p_m(x,y,t)}{\rho_\infty U_\infty^2}\psi_k\left(x,y\right)\mathrm{d}y\mathrm{d}x \tag{5}$$

With this known $Q_{m,k}\left(t\right)$, the matrices $A_{m,k}$, $B_{m,k}$, and $E_{m,k}(t)$ in Eq. 4 can be found and the unsteady aerodynamic generalized forces can be reconstructed inside the aeroelastic solver for any generalized coordinate $q_m(t)$ and $\dot{q}_m(t)$. A more detailed explanation of the method and its derivations is presented in [19], but Eqs. 6 and 7 are obtained from a CFD run with a step change on the panel deformation ($q_m(t)$), and Eq. 8. from a step change on the panel velocity ($\dot{q}_m(t)$).

$$Q_{m,k}\left(0\right) = A_{m,k}\chi \rightarrow A_{m,k} = \frac{Q_{m,k}\left(0\right)}{\chi} \tag{6}$$

$$E_{m,k}\left(t\right) = \frac{1}{\chi}\left(\dot{Q}_{m,k}\left(t\right) - \dot{Q}_{m,k}\left(0\right)\right) \tag{7}$$

$$Q_{m,k}\left(0\right) = B_{m,k}\chi \rightarrow B_{m,k} = \frac{Q_{m,k}\left(0\right)}{\chi} \tag{8}$$

For the shock configuration, an additional step is required to process the unsteady aerodynamic pressure obtained from the CFD solver, once the solution will have the steady component of the shock on the rigid panel. Because the steady pressure due to the shock impinging on the surface ($p^{steady}(x, y)$) is not affected by the enforced motion of the structure, the steady pressure distribution is removed from the unsteady Δp_m used to obtain the $A_{m,k}$, $B_{m.k}$, and $E_{m,k}(t)$

matrices, Eq. 9. The components inside the parenthesis in Eq. 9 lead to a steady component, Q_k^{Shock}, that represents the static pressure term in the model, Eq. 10.

$$\Delta p_m(x,y,t) = \frac{p_m^{CFD}(x,y,t) - p^{steady}(x,y)}{\chi} + \left(p^{steady}(x,y) - p_\infty\right) \tag{9}$$

$$Q_k^{Shock} = \iint \left(p^{steady}(x,y) - p_\infty\right) \psi_k dydx \tag{10}$$

This study will explore the case with a cavity coupled to the panel. Equation 10 is then modified to Eq. 11; another way of correlating the two expressions is to consider $p_c = p_\infty$ in Eq. 10. The cavity in this study is assumed to have an infinite depth to avoid acoustic modes affecting the dynamic response of the panel, but the model still accounts for a cavity pressure to control the Δp across both sides of the structure.

$$Q_k^{Shock} = \iint \left(p^{steady}(x,y) - p_c\right) \psi_k dydx \tag{11}$$

2.3 Modified Piston Theory (MPT): including the shock effect based on the CFD steady pressure solution

It is possible to consider the shock impingement pressure as a local and instantaneous phenomenon acting on the panel using the isentropic relations to obtain a modified version of the Linear Piston Theory terms. This approach does not consider the effect of the elastic deformation of the panel on the shock impingement location, though. Still, if one desires to consider the shock effect as a local and instantaneous behavior and use the Modified Piston Theory (MPT) as the unsteady aerodynamic model in the aeroelastic solution, Eqs. 12 to 14 present the expressions needed for it, where the local parameters are obtained based on the steady pressure distribution over a rigid panel:

$$Q_{m,k}(t) = q_m(t)\, S_{m,k} + \dot{q}_m(t)\, D_{m,k} \tag{12}$$

$$S_{m,k} = \frac{\rho_\infty U_\infty^2}{M_\infty} \iint \gamma p^{steady}(x,y)\, M_{dist}(x,y)\, \frac{\partial \psi_m(x,y)}{\partial x} \psi_k(x,y)\, dydx \tag{13}$$

$$D_{m,k} = \frac{\rho_\infty U_\infty}{M_\infty} \iint p^{steady}(x,y) \sqrt{\left(\frac{\gamma}{R_{air}T_0}\right)\left[1 + \left(\frac{\gamma-1}{2}\right) M_{dist}^2(x,y)\right]} \cdot \psi_m(x,y)\, \psi_k(x,y)\, dydx \tag{14}$$

with the Mach distribution being defined as:

$$M_{dist}(x,y) = \sqrt{\left[\left(\frac{p^{steady}(x,y)}{p_0}\right)^{-(\gamma-1)/\gamma}\right] \frac{2}{\gamma-1}} \tag{15}$$

2.4 Final Nonlinear Aeroelastic Model

The aeroelastic equation of motion to be solved in this study is presented in Eq. 16. The linear portion of the plate model is represented by the three first terms in the expression. The fourth term expresses the nonlinear stiffness due to the in-plane boundary condition imposing no in-plane displacement at the edges of the panel. The fifth term is presented in more detail in Eq. 17, and it expresses the unsteady aerodynamics coupled to the dynamic response of the panel. The sixth term expresses the static pressure differential between both sides of the panel, including the steady pressure shock.

$$M_{m,k}\ddot{q_k}\left(t\right)+C_{m,k}\dot{q_k}\left(t\right)+G^{(2)}_{m,k}q_k\left(t\right)+D^{(2)}_{m,k,s}q_k\left(t\right)q_r\left(t\right)q_s\left(t\right)+Q^{Aero}_k\left(t\right)+Q^{Shock}_k=0 \quad (16)$$

$$Q^{Aero}_k\left(t\right)=\sum_{m=1}^{N}Q^{Aero}_{m,k}\left(t\right),\ \text{and}\ Q^{Aero}_{m,k}\left(t\right)=\rho_\infty U_\infty Q_{m,k}(t) \quad (17)$$

3 RESULTS AND DISCUSSION

The equation of motion presented in Eq. 16 was solved using the Dynamic Linearized Time-domain Approach (DLTA) to compute the generalized aerodynamic forces based on an Euler solver. Table 1 presents the flow and structural parameters for the aeroelastic solution. The plate material is AISI 4140 Steel. Figure 1 shows the geometry for each shock case explored in this study, with θ being the shock wedge angle. For all three cases ($\theta = 2°$, $4°$, and $8°$), the shock impingement location was set to be the same at $x_{imp}/a \approx 0.4$. Note that the height of the wedge is selected for each θ, such that the shock impingement is nearly the same. The plate is ideally clamped to a wall and all the other three sides of the control volume are set to a pressure field with the initial conditions being presented in Table 1. In this study, the flutter boundary is sought by increasing the total pressure - and consequently the stagnation pressure and density - holding the Mach number and the total temperature (i.e. stagnation temperature) fixed, [24].

Table 1: Aerodynamic and structural parameters.

a	b	h	E	ρ	μ	T_0	M_∞
0.254 m	0.127 m	0.635 mm	200 GPa	7850 kg/m^3	0.284	295 K	2.0

The $\theta = 4°$ configuration is the same as the experimental setup presented by Brouwer et al. [2] in terms of the panel dimensions, structural properties, shock impingement location, shock wedge geometry and location. This study, however, focuses on the effect of the shock impingement presence in the dynamic response of the panel, which means that no static temperature differential will be considered. Additionally, this study focuses on exploring the response of the panel to different Δp configurations, which means the cavity pressure for this study is different from the one used in [2]. On the structural side, the aeroelastic response is sensitive to in-plane boundary deformations, having a great impact on the final panel response for this wind tunnel case, [25]. For this study, zero in-plane boundary displacement of the panel is considered for simplicity. The $\theta = 2°$ and $8°$ cases are also presented here to expand the discussion on the shock impingement case and the capabilities of the DLTA implementation. Figure 2 shows the first nine structural mode shapes considered for this study; only odd modes were used in the span direction due to the symmetry considered in Subsection 2.1.

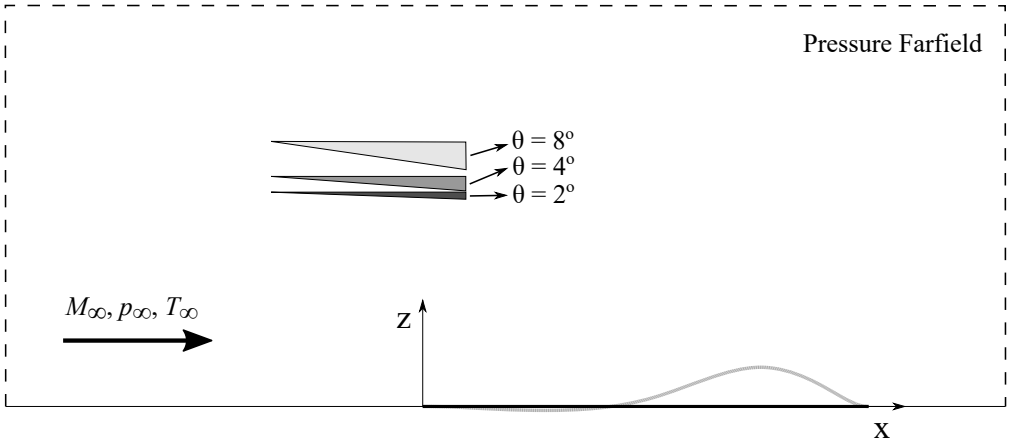

Figure 1: Schematics for the shock wedge location in the and the flexible panel location. For all cases, the shock impingement is set to be at $x_{imp}/a \approx 0.4$.

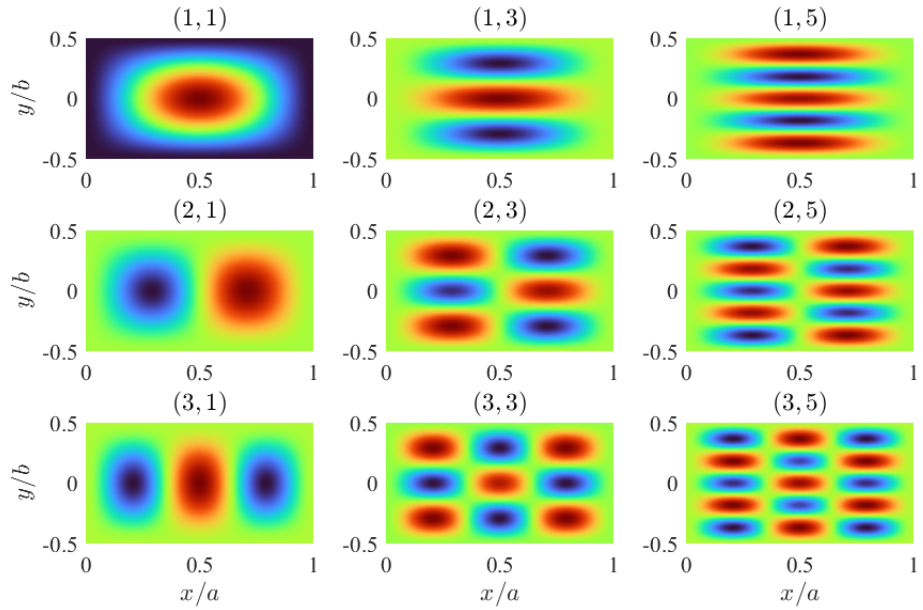

Figure 2: Mode shapes of the thin panel considered in the simulation.

Figure 3 shows the steady pressure distribution for the three shock configurations. Since the shock edge is modeled as a finite body on the control volume, there is an expansion region after it that decreases the pressure field on the panel after the shock impingement location.

3.1 Effect of the shock impingement pressure on the elastic panel and the unsteady aerodynamics

The shock impingement on the elastic panel leads to an aerodynamic steady flow nonlinearity that needs to be accounted for in the aeroelastic solution of the system. Figures 4 and 5 present three (non-dimensional) different properties obtained from a steady CFD solution for the three shock wedge cases considered in this study. First, consider the local static pressure over the panel chord, Fig. 4. Due to the pressure jump across the panel, it is expected that the total stiffness of the elastic system increases as well as the dynamic pressure for the flutter onset, mainly due to the forced deformation imposed locally on the panel from the Δp distribution,

with $\Delta p = p_{local}(x, y) - p_c$.

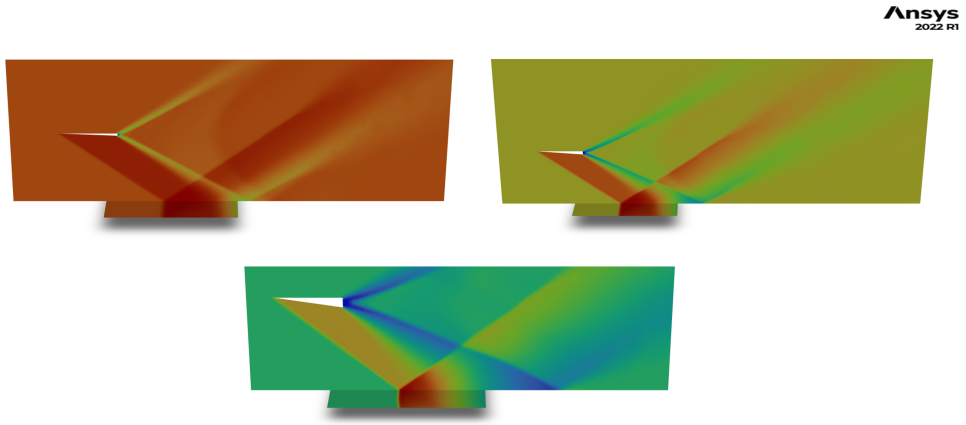

Figure 3: Steady pressure with shock impingement over a rigid panel. From left to right, first row: $\theta = 2°$ and $\theta = 4°$, second row: $\theta = 8°$.

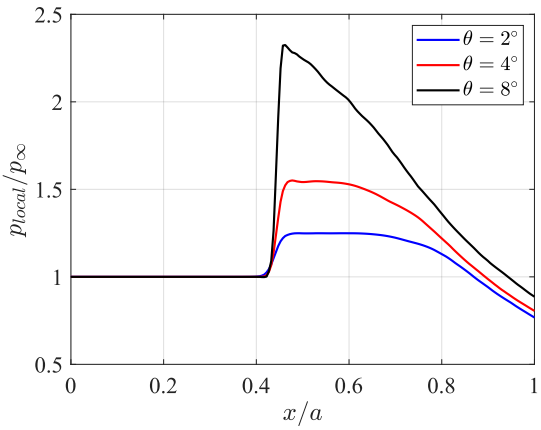

Figure 4: Local static pressure from the steady CFD solution at mid-span of the panel.

However, noting the dynamic pressure and Mach number for the same shock configurations in Fig. 5, one can also expect that the critical flutter dynamic pressure will decrease since the flow is more likely to cause an aeroelastic instability in the post-shock region, i.e. smaller Mach number and an increased local dynamic pressure. The balance between these two opposite trends (panel stiffened by the Δp effect, and a flow more likely to cause structural instability) will be explored in future sections, but this shows the complexity of studying shock configurations in the aeroelastic setting.

The benefit of using the Dynamic Linear Time-domain Approach in cases like this is the possibility of including the unsteady aerodynamic terms in the aeroelastic solution while considering nonlinear and 3D aerodynamic effects in the solution. Figures 6 and 7 show how the pressure over the panel is affected at different times due to the step-change enforced motion on the first structural mode shape of the panel, for the three different shock wedge angles. In these results, $\Delta p = p_{local}(x, y, t) - p_{steady}(x, y)$. This same behavior can not be captured using linear and local aerodynamic solutions (LPT), or an enhanced LPT using implementations based solely on steady-state flow results. For all three cases, the peak after $x_{imp}/a \approx 0.4$ represents the

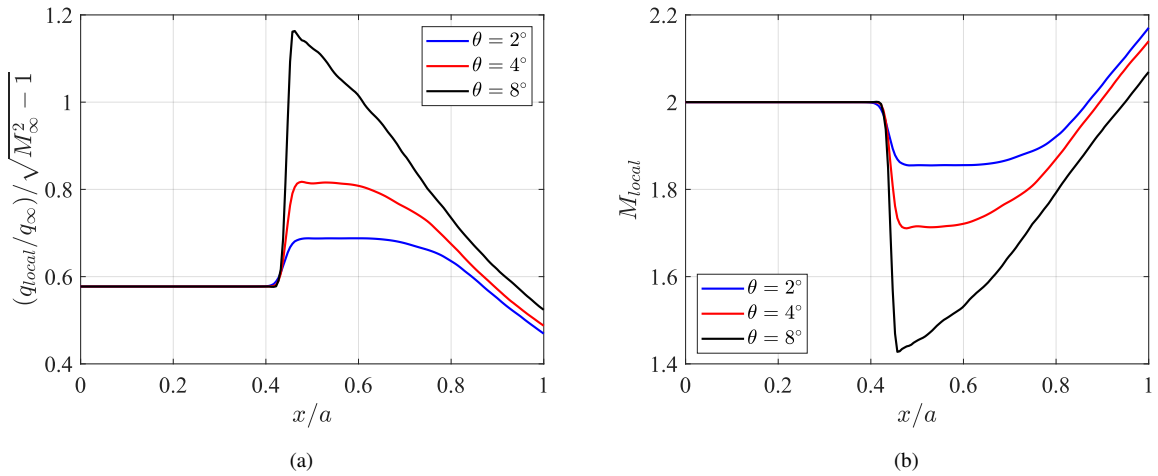

(a) (b)

Figure 5: Aerodynamic properties from the steady CFD solution at mid-span of the panel. a) Local dynamic pressure, and b) Local Mach number.

shock location moving due to the panel deformation after the first time step of the numerical aerodynamic solution, increasing as the shock wedge angle increases. The same behavior was captured experimentally in [5], where the RMS of the unsteady surface pressure signal presents a peak at the shock location.

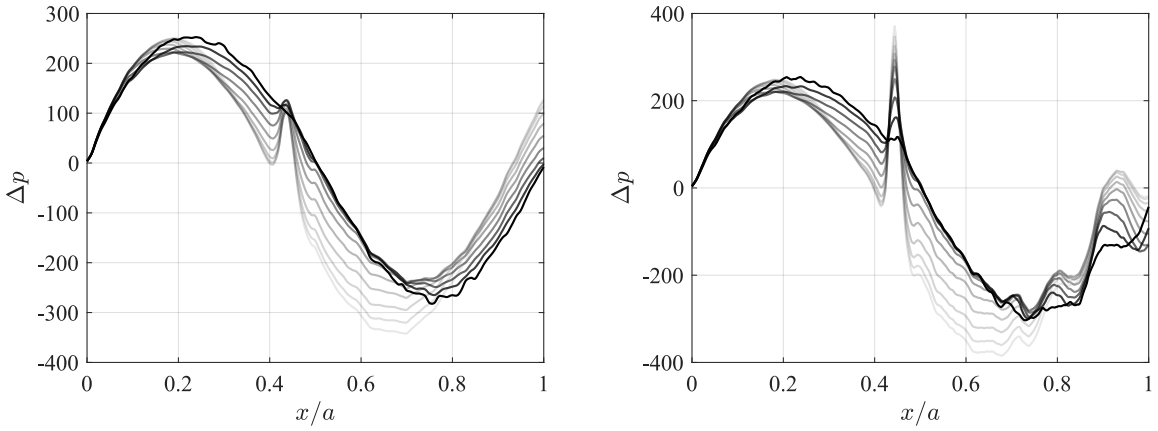

(a) (b)

Figure 6: Time lapse for the pressure distribution over the panel chord, at mid-span, given a step change in the first mode shape of the panel, for a) $\theta = 2°$, and b) $\theta = 4°$. The time step is $\Delta t = 5e{-}5s$ over 39 steps.

The shock impingement displacement will directly impact the calculations of the $E_{m,k}(t)$ since it requires the transient aerodynamic solution for each structural mode to characterize the memory and non-locality of the aerodynamics. Figure 8 presents the results for $E_{1,1}(t)$, but the same conclusions can be drawn for to the remaining modes. Figure 8a shows the aerodynamic pressure distribution over the panel after the first time step of the transient solution for the three shock wedge cases, given a step change in the first structural mode. All three shock cases show the same pressure behavior before the shock location; as expected, the main difference is the magnitude after the shock displacement, which varies as θ increases. These characteristics are enhanced for the following time steps in the CFD solution, as seen in Figs. 6 and 7, and lead to the $E_{1,1}(t)$ shown in Fig. 8b. The shape of the influence matrices for the $\theta = 2°$ and $4°$ con-

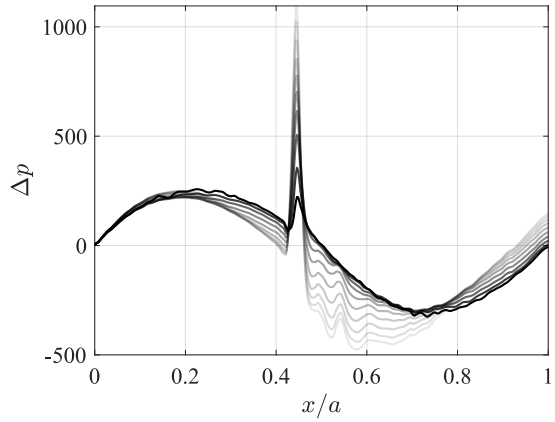

Figure 7: Time lapse for the pressure distribution over the panel chord, at mid-span, given a step change in the first mode shape of the panel, for $\theta = 8°$. The time step is $\Delta t = 5e{-}5s$ over 39 steps.

figurations are not quantitatively different from the no-shock case, which means that the shock presence does not affect the memory and non-locality of the flow. The $\theta = 8°$ configuration, however, is different due to the "oscillatory behavior" seen in the $E_{1,1}(t)$ function, even after $s = tU_\infty/a = 2$. Further study of this configuration and results is needed.

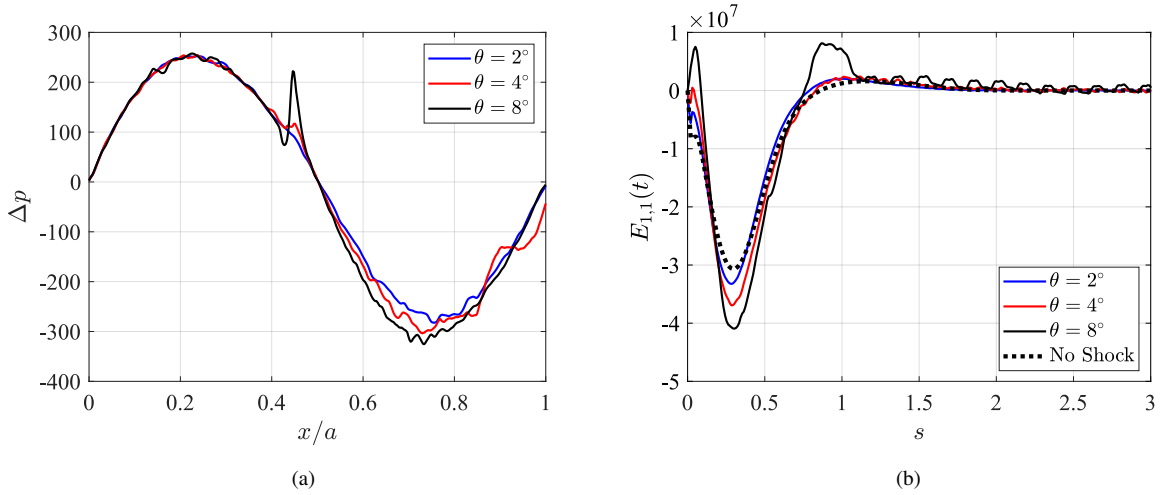

(a) (b)

Figure 8: a) Pressure distribution at mid-span and over the panel chord at the first time step after the enforced step change in the first mode shape of the panel, and b) Influence Matrix for mode (1,1) for the no shock and shock cases (all three θ values considered).

3.2 Instability Mechanism: steady static pressure distribution vs. unsteady pressure coupling with the flexible structure

One can explore different scenarios for the static pressure term, and obtain some conclusions from this particular instability mechanism and its relationship to the steady shock pressure distribution. Three different scenarios for the aeroelastic system will be explored, in addition to the three different shock angles. For all cases, the elastic panel has one side towards the aerodynamic flow and the other towards an acoustic cavity with infinite depth. Figure 9 illustrates each one of the cases considered: Case 1) Q_k^{Shock} is based on the shock distribution p_{shock} and a cavity pressure $p_c = p_\infty$: the resulting static pressure differential will have $\Delta p \neq 0$ only for the post-shock region of the panel; Case 2) Q_k^{Shock} is based on the shock distribution p_{shock} and

a cavity pressure $p_c = \langle\langle p_{shock}(x,y)\rangle\rangle$: this configuration assumes that $\Delta p \neq 0$ for the entire area of the panel, for a given cavity pressure that is above the freestream static pressure; and Case 3) Q_k^{Shock} is based on the shock distribution p_{shock} and a cavity pressure $p_c = p_{shock}$: this configuration assumes that the cavity pressure has the same pressure profile as the aerodynamic steady solution with the shock impingment, leading to $\Delta p = 0$ for the entire area of the panel. Although the last case is not realistic (it is not possible to replicate this configuration in a wind tunnel experiment) it provides the opportunity to assess the influence of the static pressure differential in the dynamic response of the elastic panel, and how it can influence the instability mechanism.

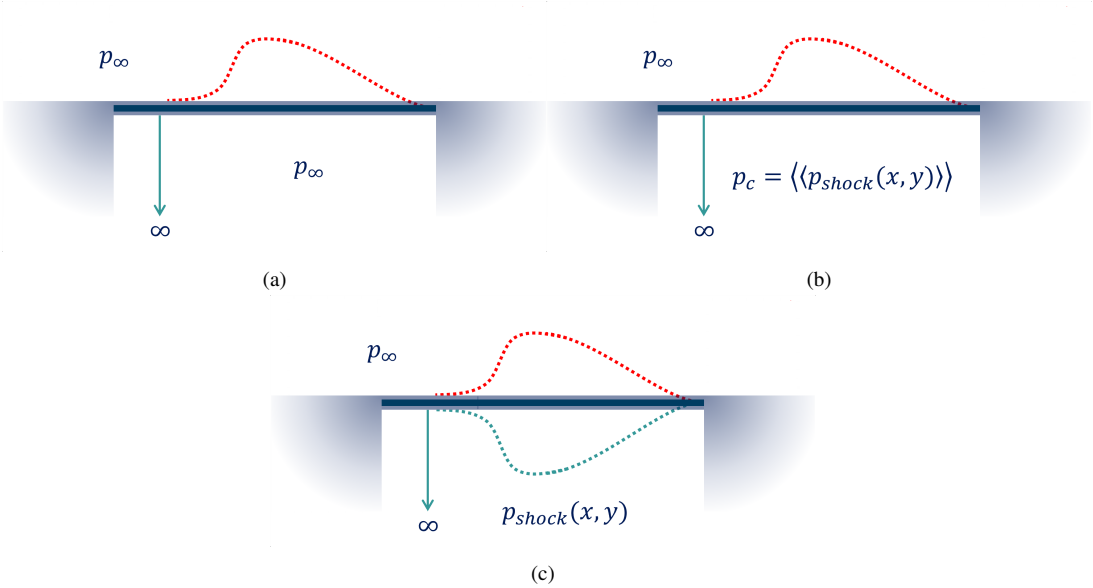

Figure 9: Schematics of different configurations for the aeroelastic system explored in this study. a) Case (1): $p_c = p_\infty$, with $\Delta p \neq 0$; b) Case (2) $p_c = \langle\langle p_{shock}(x,y)\rangle\rangle$, with $\Delta p \neq 0$; and c) Case (3): $p_c = p_{shock}(x,y)$, with $\Delta p = 0$.

3.2.1 Shock Wedge $\theta = 2°$

Figure 10 presents the RMS of the dynamic displacement for the panel ($\hat{w}$ relative to the mean deformation) normalized by the panel thickness, and the reduced frequency at the same location, for the $\theta = 2°$ configuration. Depending on the Q_k^{Shock} case, the panel peak displacement is located at a different position over the chord. The respective response location is indicated in Table 2 and it is valid for all results presented in this study.

Table 2: Location of the peak displacement for each Q_k^{Shock} case.

Q_k^{Shock} case	x/a
"*w/o shock*", $\Delta p = 0$	0.75
$p_c = p_\infty$, $\Delta p \neq 0$	0.60
$p_c = \langle\langle p_{shock}(x,y)\rangle\rangle$, $\Delta p \neq 0$	0.65
$p_c = p_{shock}(x,y)$, $\Delta p = 0$	0.75

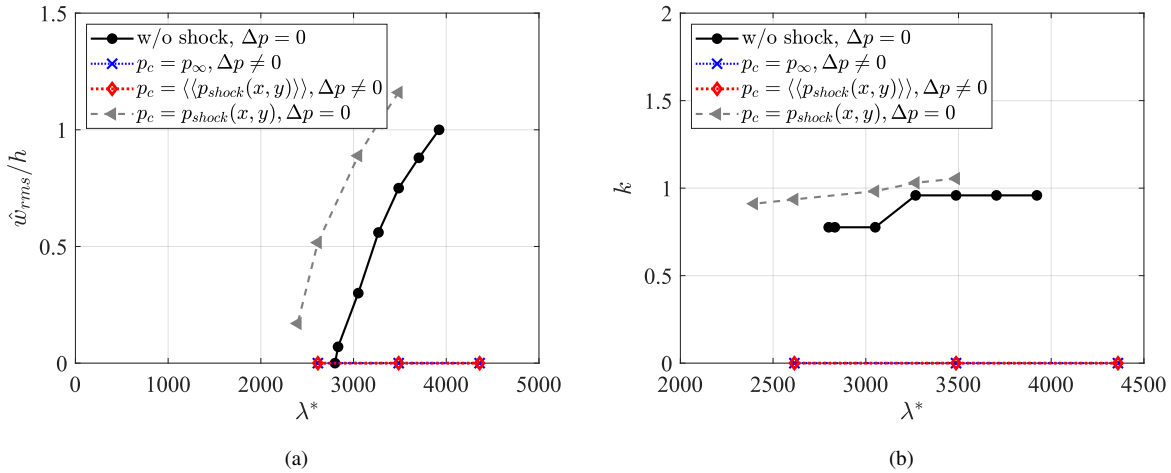

Figure 10: Aeroelastic result for the $\theta = 2°$ shock and no-shock cases. a) RMS of $\hat{w}(t)/h$ (LCO), and b) reduced frequency.

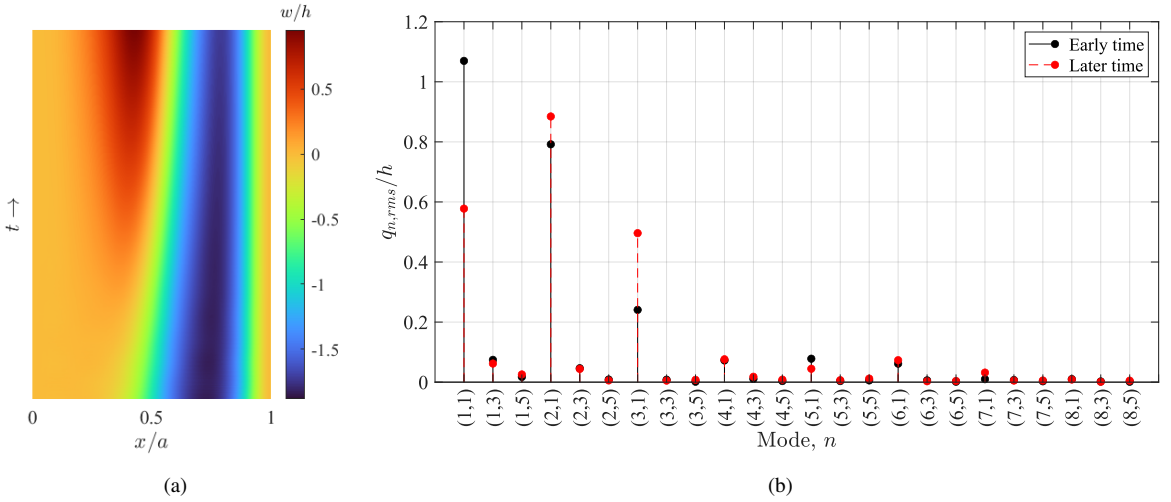

Figure 11: Aeroelastic result with $p_c = p_\infty$ ($\Delta p \neq 0$), $\lambda^* = 3486.76$, $\theta = 2°$. a) Mid-span deformation time history, and b) RMS of the full panel response modal composition, $(\hat{q}_n(t) + q_n^{static})_{rms}/h$.

For all values of λ^* considered, an LCO behavior is only seen when $\Delta p = 0$, which indicates that for shock wedge angle, the static pressure term $Q_k^{Shock} \neq 0$ dominates the response by suppressing the flutter onset. Interestingly, however, when $\Delta p \neq 0$, although the final dynamic response of the panel is a static deformation due to the static pressure term, the unsteady aerodynamics shifts the deformation shape of the panel from the "first mode-shape", since the deformation is formed with the localized pressure gradient from the shock impingement, to a "second mode-shape", as presented in Fig. 11a. This shift in the deformation shape is also seen in the modal composition of the response at a later time, Fig. 11b, where one can see that the participation of the $(2,1)$ mode, as well as the $(3,1)$ mode, becomes as relevant to the final response as the $(1,1)$ mode.

3.2.2 Shock Wedge $\theta = 4°$

As the shock wedge angle increases, the dynamic response of the plate starts to have LCO behavior even for $\Delta p \neq 0$. Figure 12 shows the RMS of the dynamic deformation of the panel

$\hat{w}$ and the RMS for the panel full deformation for $\theta = 4°$, following the same convention as previously mentioned in terms of peak location, Table 2. All cases of Q_k^{Shock} now show an LCO, with the flutter on-set starting at different λ^*. As the free stream dynamic pressure increases further beyond the onset flutter, however, the LCO is suppressed for the $\Delta p \neq 0$ configurations once the static pressure term stiffens the panel enough. In terms of the reduced frequency, Fig. 13, Cases (1) and (2) present higher frequencies than the "no shock" configuration and Case (3), $\Delta p = 0$. Figures 14 to 16 show the mid-span deformation time history for the same value of λ^* and the three different cases for the cavity pressure, p_c, as well as the modal composition for each case.

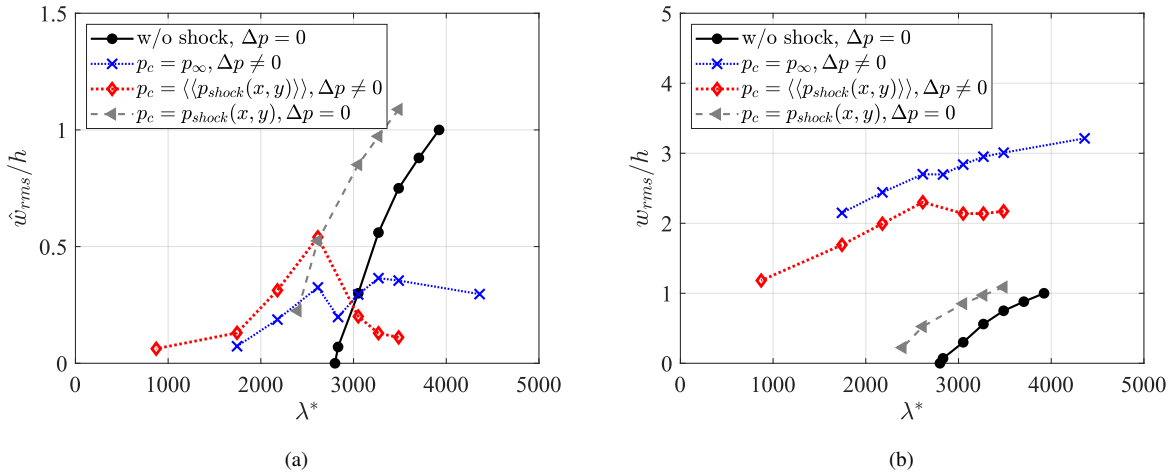

Figure 12: Aeroelastic result for the $\theta = 4°$ shock and no-shock cases. a) RMS of $\hat{w}(t)/h$ (LCO), and b) RMS of the panel response including the mean deformation, $(\hat{w}(t) + w_{static})_{rms}/h$.

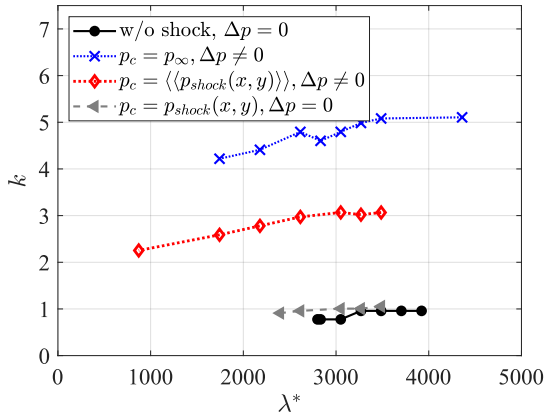

Figure 13: Reduced frequency of the panel deformation, $\theta = 4°$.

In terms of the modal composition of the responses presented in Figs. 14 to 16, one can see that when considering the contribution of the total panel response, i.e. including the static deformation of the panel due to the Δp and the dynamic deformation of the panel around the static deformation $((\hat{q}_n(t) + q_n^{static})_{rms}/h)$, the first and second modes in the chord direction, $(1,1)$ and $(2,1)$, dominate the response. But when the modal weights are considered only for the dynamic oscillation of the panel around the mean deformation $(\hat{q}_{n,rms}(t)/h)$, higher modes dominate the response, which correlates with the high reduced frequencies seen in Fig.

13. Figure 16 is a special case. When $\Delta p = 0$, there is no static deformation of the panel, leading to the same modal contribution when assessing $\hat{q}_{n,rms}(t)$ and $(\hat{q}_n(t) + q_n^{static})_{rms}$. For this case, the oscillation is seen only at the post-shock region, which is consistent with the previous observation on the increase in the local dynamic pressure and decrease of the Mach number in this region, Fig. 5.

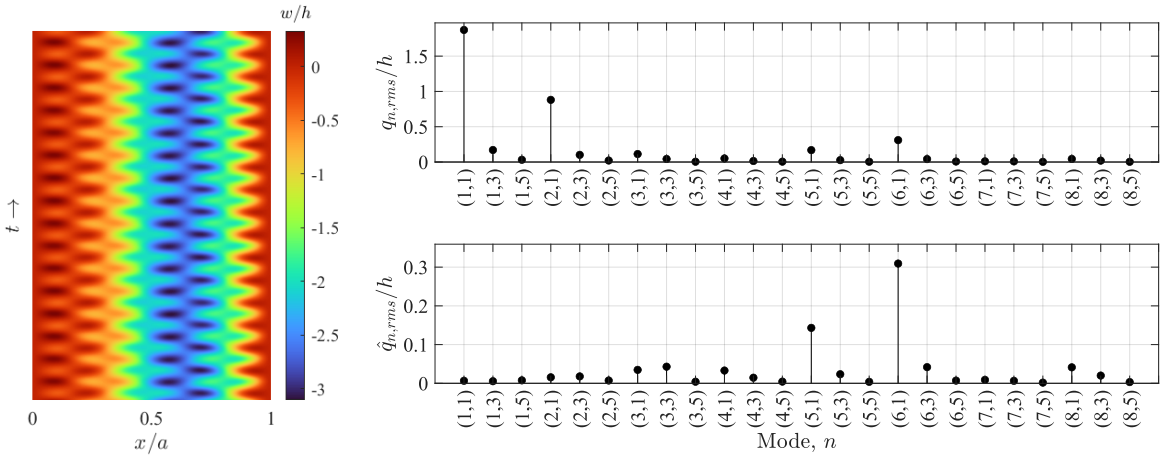

(a) (b)

Figure 14: Aeroelastic result with $p_c = p_\infty$ ($\Delta p \neq 0$), $\lambda^* = 3486.76$, $\theta = 4°$. a) Mid-span deformation time history, and b) RMS of the full panel response modal composition, $(\hat{q}_n(t) + q_n^{static})_{rms}/h$, (top figure) and the dynamic deformation, $\hat{q}_{n,rms}(t)/h$, (lower figure).

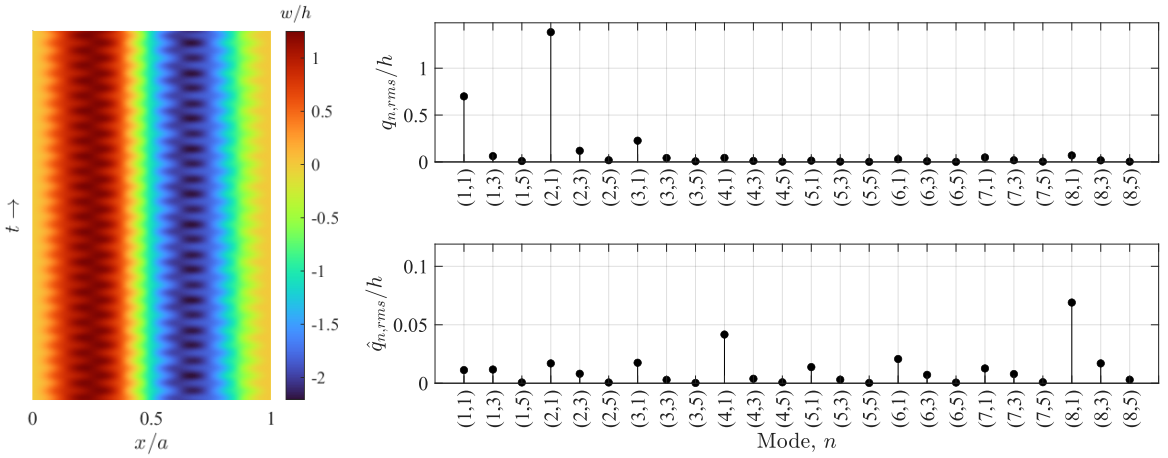

(a) (b)

Figure 15: Aeroelastic result with $p_c = \langle\langle p_{shock}(x,y)\rangle\rangle$ ($\Delta p \neq 0$), $\lambda^* = 3486.76$, $\theta = 4°$. a) Mid-span deformation time history, and b) RMS of the full panel response modal composition, $(\hat{q}_n(t) + q_n^{static})_{rms}/h$, (top figure) and the dynamic deformation, $\hat{q}_{n,rms}(t)/h$, (lower figure).

Although the panel response when $\Delta p \neq 0$ is dominated by high-frequency content, the LCO is mostly periodic in the range of λ^* assessed. Figure 17a presents the phase-plane plot of the same configuration presented in Fig. 14 once the LCO is reached. At this value of λ^*, the LCO response is already being suppressed by the increase in the static pressure differential, but when looking at a lower λ^* condition. Fig. 17b, it is possible to note a clearer oscillatory behavior,

especially after the shock-impingment location. Figure 17b presents the mid-span deformation time history with $p_c = \langle\langle p_{shock}(x,y)\rangle\rangle$ ($\Delta p \neq 0$), the same configuration in Fig. 15 but with a lower λ^*. The comparison between these two results shows how stiffened the panel becomes with a bigger λ^* and how that affects the dynamics of the system.

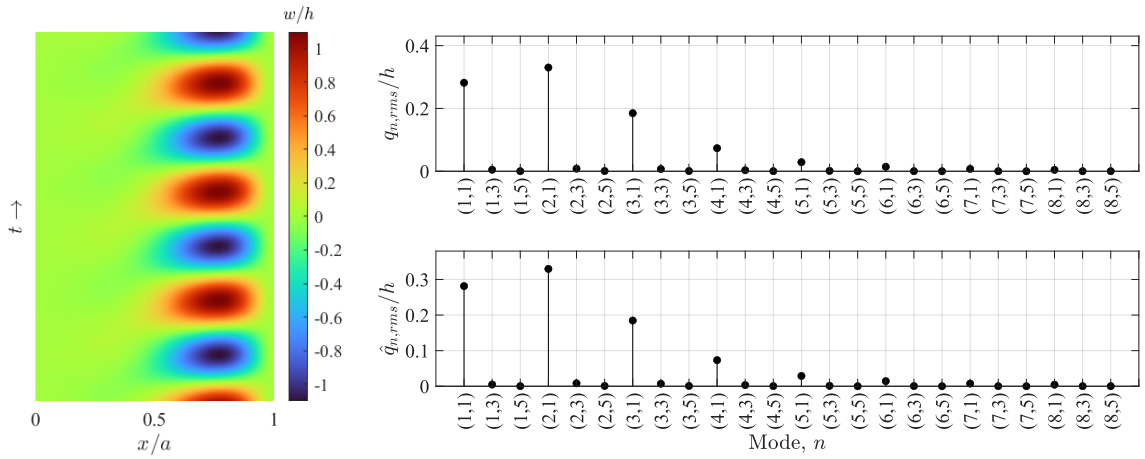

(a) (b)

Figure 16: Aeroelastic result with $p_c = p_{shock}(x,y)$ ($\Delta p = 0$), $\lambda^* = 3486.76$, $\theta = 4°$. a) Mid-span deformation time history, and b) RMS of the full panel response modal composition, $(\hat{q}_n(t) + q_n^{static})_{rms}/h$, (top figure) and the dynamic deformation, $\hat{q}_{n,rms}(t)/h$, (lower figure).

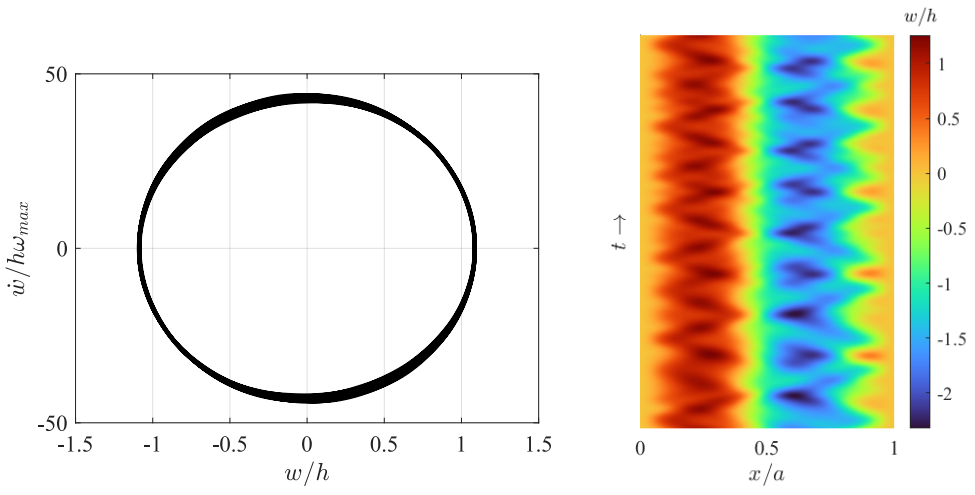

(a) (b)

Figure 17: a) Phase-plane plot of the response presented in Fig. 14, $p_c = p_\infty$ ($\Delta p \neq 0$), $\lambda^* = 3486.76$, $\theta = 4°$, and b) Mid-span deformation time history with $p_c = \langle\langle p_{shock}(x,y)\rangle\rangle$ ($\Delta p \neq 0$), $\lambda^* = 2615.07$, $\theta = 4°$.

3.2.3 Shock Wedge $\theta = 8°$

For $\theta = 8°$, the dynamic response of the plate becomes more chaotic and difficult to characterize. Figure 18 presents the RMS of the dynamic deformation of the panel and the RMS for panel full deformation with $\theta = 8°$. Once again, LCO is seen for all p_c cases, but with the flutter onset earlier than the no-shock configuration. For the $\Delta p \neq 0$ cases, however, the identification of the peak deformation is also more challenging. The content of high frequency when $\Delta p \neq 0$ was already presented in Subsection 3.2.2, but the chaotic behavior of the panel response becomes

more intense for higher θ's.

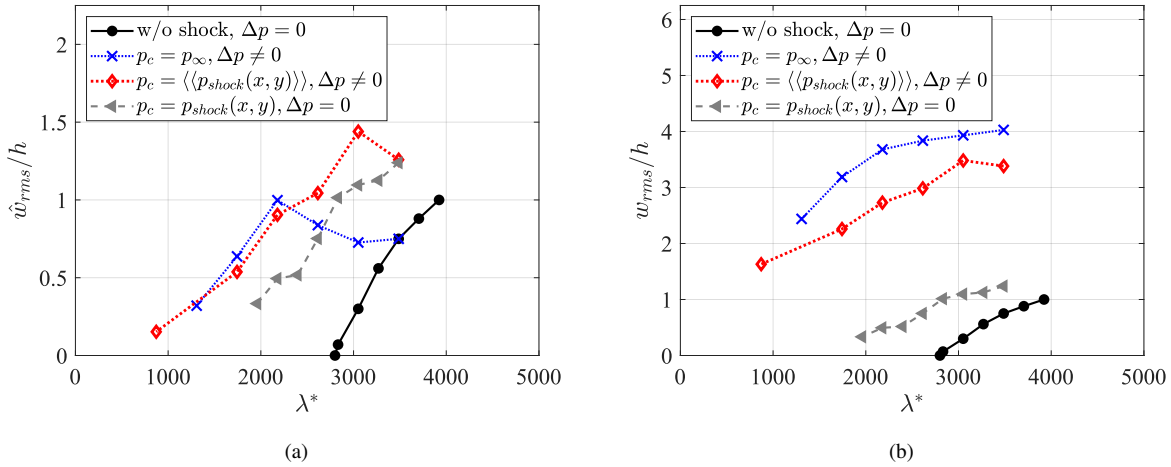

Figure 18: Aeroelastic result for the $\theta = 8°$ shock and no-shock cases. a) RMS of $\hat{w}(t)/h$ (LCO), and b) RMS of the panel response with the mean deformation, $(\hat{w}(t) + w_{static})_{rms}/h$.

Figure 19 presents the reduced frequency for the panel when $\theta = 8°$. As one can see the results are more complex than the $\theta = 4°$ case, both when $\Delta p \neq 0$ and $\Delta p = 0$. Although the same stiffening effect with the increase of the λ^* occurs, the modal composition for all the results has more than one or two dominant frequencies, leading to a chaotic LCO and the difficulty in computing one value for k. Figure 20 presents the phase-plane plots for cases (1) and (2), i.e. $p_c = p_\infty$ and $\langle\langle p_{shock}(x,y)\rangle\rangle$ respectively, $(\Delta p \neq 0)$ at the same λ^*. One hypothesis for this chaotic behavior for high θ is the "oscillatory behavior" seen in the Influence Function $E_{m,k}(t)$ for $\theta = 8°$, Fig. 8b. As previously mentioned, further study is needed for this configuration to assess if this sustained oscillation in the $E_{m,k}(t)$ functions characterizes a physical fluid instability, or if this shock wedge configuration requires a different numerical setup to obtain the unsteady aerodynamic matrices, such as a refined mesh or a different aerodynamic solver.

Figure 21 presents the mid-span deformation time history and the RMS of the modal composition of the response for the same configuration presented in Fig. 20b. It illustrates the complexity of the dynamic panel deformation and the dominance of at least four mode shapes in the dynamic deformation of the panel around the static deformation due to Δp.

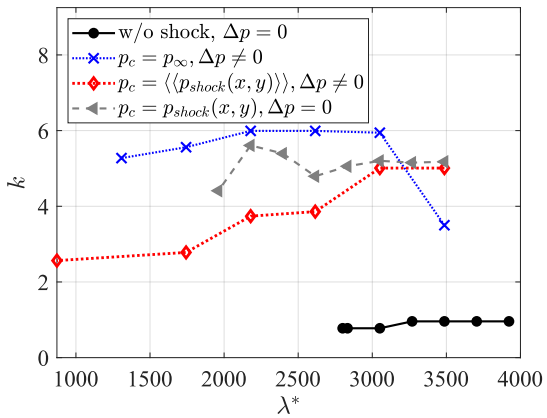

Figure 19: Reduced frequency of the panel deformation, $\theta = 8°$.

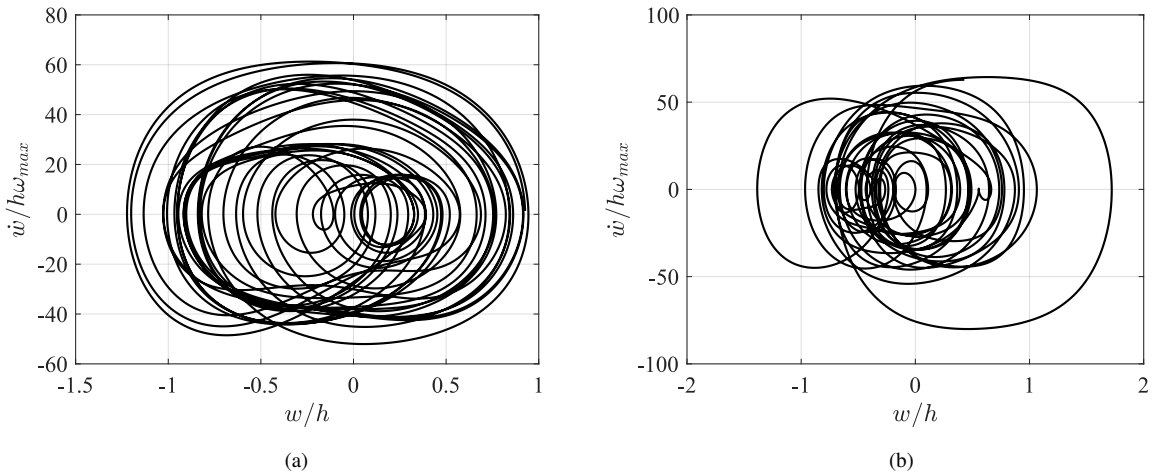

Figure 20: Phase-plane plot of the response in the last 0.01s of the simulated response a) $p_c = p_\infty$ ($\Delta p \neq 0$), $\lambda^* = 3486.76$, $\theta = 8°$, and b) $p_c = \langle\langle p_{shock}(x,y)\rangle\rangle$ ($\Delta p \neq 0$), $\lambda^* = 3486.76$, $\theta = 8°$.

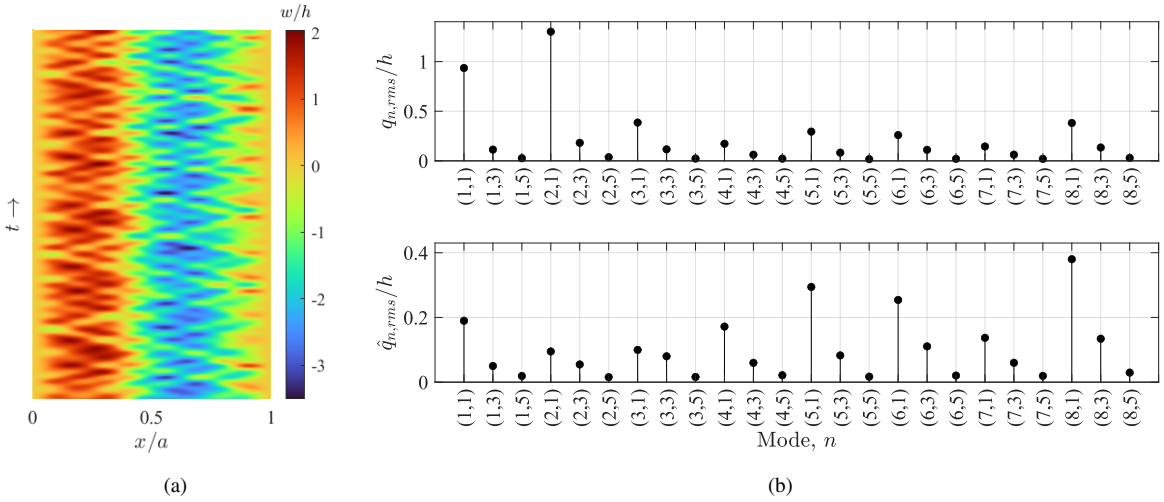

Figure 21: Aeroelastic result with $p_c = \langle\langle p_{shock}(x,y)\rangle\rangle$ ($\Delta p \neq 0$), $\lambda^* = 3486.76$, $\theta = 8°$. a) Mid-span deformation time history, and b) RMS of the full panel response modal composition, $(\hat{q}_n(t) + q_n^{static})_{rms}/h$, (top figure) and the dynamic deformation, $\hat{q}_{n,rms}(t)/h$, (lower figure).

3.3 Impingent Shock as a Local and Instantaneous Behavior: Using the Modified Linear Piston Theory as the Unsteady Aerodynamic Model

The Dynamic Linearized Time-domain Approach method allows the inclusion and assessment of the unsteady aerodynamics computed by a CFD solver into the aeroelastic simulation without the need to run a full CFD solver for each aeroelastic simulation. However, it is worth comparing this new method with a more traditional one, such as the Piston Theory, or for the case of a shock impingement, the Modified Piston Theory (MPT), introduced in Section 2.3. It is possible to compare both methods in the current study since all configurations use $M_\infty = 2.0$, although it was already pointed out in another study [26] that for the effective aspect ratio of $b/a = 0.5$, three-dimensional effects play an important role in the final unsteady aerodynamics even for $M_\infty = 2.0$, which are not included in the Piston Theory formulation. The comparison presented here assumes that the nonlinear effect due to the shock impingement will dominate

over the three-dimensional effects, once the pressure distribution at the mid-span of the panel is assumed uniform in the span direction of the panel when computing the MPT matrices.

Figure 22 presents the comparison between the Modified Piston Theory and the Dynamic Linearized Time-domain Approach with an Euler solver for two different scenarios. First, the comparison is on the dynamic deformation of the panel, with $p_c = p_{shock}(x, y)$, $\Delta p = 0$. One can see from Fig. 22a that the MPD overestimates the flutter onset for all shock angles, while the DLTA presents a smaller value for flutter onset. Interestingly, similar LCO results are seen for $\theta = 2°$ and $4°$ but not $\theta = 8°$ when $\Delta p = 0$. The similarity for $\theta = 2°$ and $4°$ can be traced back to Fig. 5, since the values for the dynamic pressure and the Mach number after the shock are not much different between the two shock angles, both in terms of magnitude and distribution. However, for $\theta = 8°$, the properties are distinct from the first two shock angles, with a peak in the dynamic pressure that is almost twice the value seen for $\theta = 2°$, combined with the behavior already discussed for the $E_{m,k}(t)$ function.

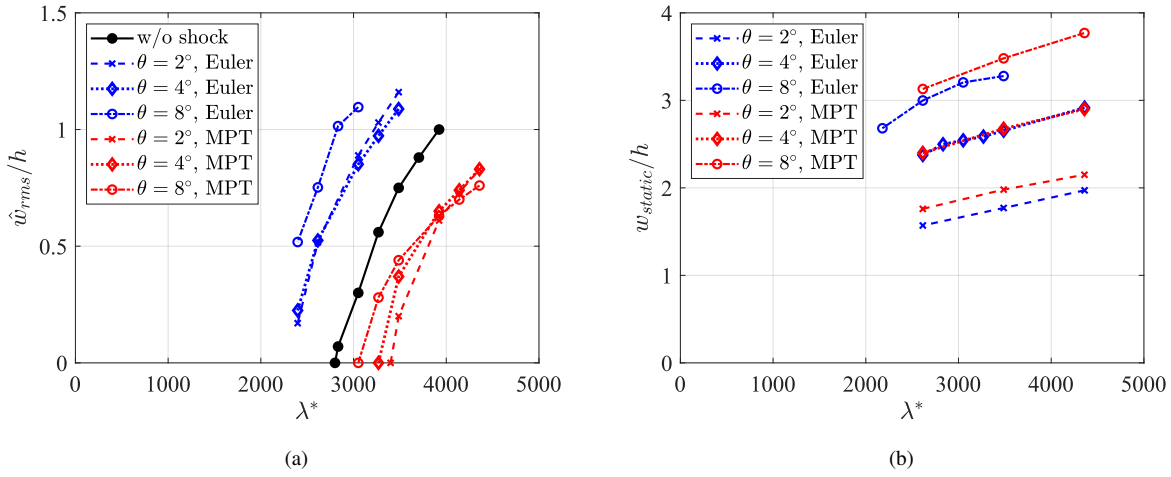

(a) (b)

Figure 22: Comparison between MPT and DLTA with an Euler solver. a) RMS of $\hat{w}(t)/h$ (LCO) with $p_c = p_{shock}(x, y)$, $\Delta p = 0$, and b) Static panel response due to the static pressure differential $\Delta p \neq 0$, $p_c = p_\infty$. All points were obtained at $x/a = 0.75$.

The second scenario for comparison is presented in Fig. 22b, where only the static panel response due to the static pressure differential is presented. This comparison is motivated by the fact that, when using MPT as the unsteady aerodynamic model, all values of λ^* for all three values of θ led to a static deformation. This can be attributed to the local flow characteristic of the Piston Theory, which makes the static term stiffen the panel with a much lower λ^* than it did when using the DLTA implementation. But Fig. 22b indicates that even with the lack of LCO when using the MPT in the aeroelastic formulation, the method can successfully obtain the same static deformation for the panel for all shock angles in this study. This indicates that, although the local solution of the MPT overpredicts the flutter onset when having a shock impingement of the panel, it can model the panel behavior in pre-flutter λ^*. This is particularly useful when correlating experimental results that are outside the flutter instability zone. However, this is not true for correlation with experimental results when LCO is seen. Figure 23 shows the corresponding reduced frequencies.

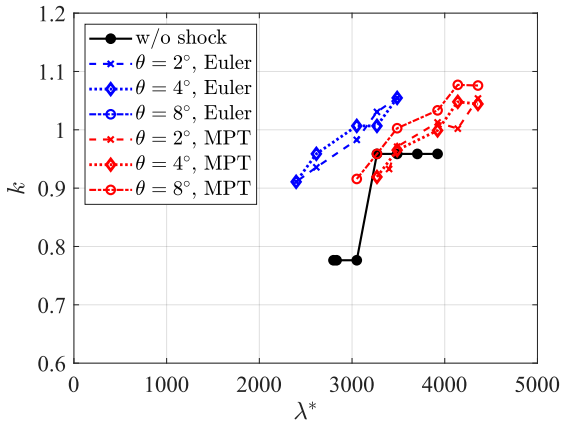

Figure 23: Reduced frequency of the panel deformation, using MPT and DLTA with an Euler solver.

4 CONCLUSIONS AND NEXT STEPS

The effect of unsteady aerodynamics in panel flutter considering a shock impinging on the surface is considered in this study to explore the capabilities of the Dynamic Linearized Time-domain Approach using an inviscid CFD solver. In terms of the unsteady aerodynamic modeling, it was shown that the DLTA allows the consideration of the shock displacement due to the panel deformation in time. The study also introduced a new perspective on the effects of the shock impingement and the instability mechanisms on a flexible panel in a $M_\infty = 2.0$ flow, exploring the effect of the static pressure distribution over the panel and the important role it plays in the flutter onset for the different shock-wedge angles. Three shock wedge angles were considered in this study, and the complexity of this type of aeroelastic modeling was noted. Relevant next steps would include the following:

- Expand the methodology to include viscous effects using RANS CFD solutions, with and without a shock impingement case.
- Investigate the unsteady aerodynamic modeling using DLTA for higher shock wedge angles, particularly for the cases where there is separation of the flow.
- Vary the position of the shock impinging on the panel.
- Make a comparison of computational results to available experimental results.

5 REFERENCES

[1] Brouwer, K. R., Perez, R. A., Beberniss, T. J., et al. (2021). Experiments on a thin panel excited by turbulent flow and shock/boundary-layer interactions. *AIAA Journal*, 59(7), 2737–2752. doi:10.2514/1.J060114.

[2] Brouwer, K. R., Perez, R., Beberniss, T. J., et al. Aeroelastic experiments and companion computations assessing the impact of impinging shock sweep. In *AIAA SCITECH 2023 Forum*. doi:10.2514/6.2023-0945.

[3] DeBonis, J. R., Oberkampf, W. L., Wolf, R. T., et al. (2012). Assessment of computational fluid dynamics and experimental data for shock boundary-layer interactions. *AIAA Journal*, 50(4), 891–903. doi:10.2514/1.J051341.

[4] Brouwer, K. R., Perez, R. A., Beberniss, T. J., et al. (2023). Aeroelastic response of a thin panel excited by a separated shock–boundary layer interaction. *Physics of Fluids*, 35(12), 125153. ISSN 1070-6631. doi:10.1063/5.0175161.

[5] Brouwer, K. R., Perez, R., Beberniss, T. J., et al. Surface pressure measurements and predictions in shock-dominated flows. In *AIAA AVIATION 2023 Forum*. doi:10.2514/6.2023-4134.

[6] Spottswood, S. M., Beberniss, T. J., Eason, T. G., et al. (2019). Exploring the response of a thin, flexible panel to shock-turbulent boundary-layer interactions. *Journal of Sound and Vibration*, 443, 74–89. ISSN 0022-460X. doi:https://doi.org/10.1016/j.jsv.2018.11.035.

[7] Poplingher, L., Touati, N., Raveh, D. E., et al. Investigation of the aeroelastic response of a compliant panel. In *AIAA SCITECH 2024 Forum*. doi:10.2514/6.2024-2444.

[8] Kokkinakis, I. W., Drikakis, D., Michael Spottswood, S., et al. (0). Aeroacoustic loading of impinging supersonic boundary-layer interaction on statically deformed surfaces. *AIAA Journal*, 0(0), 1–18. doi:10.2514/1.J063702.

[9] Currao, G. M. D., McQuellin, L. P., Neely, A. J., et al. (2021). Hypersonic oscillating shock-wave/boundary-layer interaction on a flat plate. *AIAA Journal*, 59(3), 940–959. doi:10.2514/1.J059590.

[10] Vasconcelos, P. B., McQuellin, L. P., Krishna, T., et al. Experimental study of hypersonic fluid-structure interactions on an inclined clamped-free-clamped-free compliant panel. In *ASCEND 2021*. doi:10.2514/6.2021-4232.

[11] Brouwer, K. R. and McNamara, J. J. (2019). Enriched piston theory for expedient aeroelastic loads prediction in the presence of shock impingements. *AIAA Journal*, 57(3), 1288–1302. doi:10.2514/1.J057595.

[12] Currao, G. M. D., Neely, A. J., Kennell, C. M., et al. (2019). Hypersonic fluid–structure interaction on a cantilevered plate with shock impingement. *AIAA Journal*, 57(11), 4819–4834. doi:10.2514/1.J058375.

[13] Visbal, M. (2014). Viscous and inviscid interactions of an oblique shock with a flexible panel. *Journal of Fluids and Structures*, 48, 27–45. ISSN 0889-9746. doi:https://doi.org/10.1016/j.jfluidstructs.2014.02.003.

[14] Boyer, N. R., McNamara, J. J., Gaitonde, D. V., et al. Study on shock-induced panel flutter in 3-d inviscid flow. In *58th AIAA/ASCE/AHS/ASC Structures, Structural Dynamics, and Materials Conference*. doi:10.2514/6.2017-0404.

[15] Boyer, N. R., McNamara, J., Gaitonde, D., et al. (2018). Features of shock-induced panel flutter in three-dimensional inviscid flow. *Journal of Fluids and Structures*, 83, 490–506. ISSN 0889-9746. doi:https://doi.org/10.1016/j.jfluidstructs.2018.10.001.

[16] Laguarda, L., Hickel, S., Schrijer, F. F. J., et al. (2024). Shock-wave/turbulent boundary-layer interaction with a flexible panel. *Physics of Fluids*, 36(1), 016120. ISSN 1070-6631. doi:10.1063/5.0179082.

[17] Johnson, C., Piccolo Serafim, L., Oefelein, J. C., et al. Prediction of sbli induced flexible panel motion using wall-modeled les coupled to an aeroelastic solver. In *AIAA SCITECH 2024 Forum*. doi:10.2514/6.2024-1155.

[18] Hiller, B. R., Frink, N. T., Silva, W. A., et al. (2020). Aeroelastic indicial response reduced-order modeling for flexible flight vehicles. *Journal of Aircraft*, 57(3), 469–490. doi: 10.2514/1.C035646.

[19] Piccolo Serafim, L. and Dowell, E. H. Dynamically linearized euler time-domain approach with shock impingement for lco prediction for an elastic panel. In *AIAA SCITECH 2024 Forum*. doi:10.2514/6.2024-0189.

[20] Ballhaus, W. F. and Goorjian, P. M. (1978). Computation of unsteady transonic flows by the indicial method. *AIAA Journal*, 16(2), 117–124. doi:10.2514/3.60868.

[21] Freydin, M., Dowell, E. H., Whalen, T. J., et al. (2020). A theoretical computational model of a plate in hypersonic flow. *Journal of Fluids and Structures*, 93, 102858. ISSN 0889-9746. doi:https://doi.org/10.1016/j.jfluidstructs.2019.102858.

[22] Freydin, M. and Dowell, E. H. (2021). Nonlinear theoretical aeroelastic model of a plate: Free to fixed in-plane boundaries. *AIAA Journal*, 59(2), 658–672. doi:10.2514/1.J059551.

[23] Leissa, A. W. (1969). *Vibration of Plates*. NASA Report No. SP-160.

[24] Dowell, E. H. (1975). *Aeroelasticity of plates and shells*. Leyden, Noordhoff International.

[25] Piccolo Serafim, L., Freydin, M., and Dowell, E. H. (2023). Correlation of supersonic wind tunnel measurements with a nonlinear aeroelastic theoretical/computational model of a thin plate. *Journal of Fluids and Structures*, 122, 103981. ISSN 0889-9746. doi: https://doi.org/10.1016/j.jfluidstructs.2023.103981.

[26] Piccolo Serafim, L., Freydin, M., and Dowell, E. H. (2023). Flutter and limit-cycle oscillations of a panel using unsteady potential flow aerodynamics. *AIAA Journal*, 61(11), 5009–5017. doi:10.2514/1.J062943.

ACKNOWLEDGMENTS

This work is supported by a U.S. Air Force Office of Scientific Research (AFOSR) grant with Dr. Sarah Popkin and Dr. Martin Schmidt as the program directors, originally, and now with Dr. Gregg Abate as the program director.

COPYRIGHT STATEMENT